

**Mapping Static Core-Holes and Ring-Currents with X-ray
Scattering**

Journal:	<i>Faraday Discussions</i>
Manuscript ID	FD-ART-11-2020-000124.R1
Article Type:	Paper
Date Submitted by the Author:	21-Dec-2020
Complete List of Authors:	Carrascosa, Andrés; Brown University Yang, Mengqi; Louisiana State University, Chemistry Yong, Haiwang; Brown University, Ma, Lingyu; Brown University Kirrander, Adam; University of Edinburgh, School of Chemistry Weber, Peter; Brown University, Dept. of Chemistry Lopata, Kenneth; Louisiana State University, Chemistry; Louisiana State University, Center for Computation and Technology

Cite this: DOI: 00.0000/xxxxxxxxxx

Mapping Static Core-Holes and Ring-Currents with X-ray Scattering

Andrés Moreno Carrascosa ^a, Mengqi Yang ^b, Haiwang Yong ^a, Lingyu Ma ^a, Adam Kirrander ^c, Peter M. Weber ^{*a} and Kenneth Lopata ^{*b,d}

Received Date

Accepted Date

DOI: 00.0000/xxxxxxxxxx

Measuring the attosecond movement of electrons in molecules is challenging due to the high temporal and spatial resolutions required. X-ray scattering-based methods are promising, but many questions remain concerning the sensitivity of the scattering signals to changes in density, as well as the means of reconstructing the dynamics from these signals. In this paper, we present simulations of stationary core-holes and electron dynamics following inner-shell ionization for oxazole molecule. Using a combination of time-dependent density functional theory simulations along with X-ray scattering theory, we demonstrate that the sudden core-hole ionization produces a significant change in the X-ray scattering response and how the electron currents across the molecule should manifest as measurable modulations to the time dependent X-ray scattering signal. This suggests that X-ray scattering is a viable probe for measuring electronic processes at times scales faster than nuclear motion.

1 Introduction

The recent emergence of ultra-short pulsed X-ray free-electron lasers (XFELs) has introduced new tools to study chemical processes, in particular photochemical or photophysical events. X-ray scattering experiments, limited in the past to crystalline samples, have become possible for all states of matter, and even low density, gaseous samples can be now studied as a consequence of the high peak brightness of these new X-ray sources. The spatial resolution and the short duration of these X-ray pulses has enabled gas-phase time-resolved X-ray scattering experiments where the time evolution of the electronic¹ and nuclear^{2,3} degrees of freedom in the system can be measured after ionization or excitation. These advances have made time-resolved X-ray scattering a useful tool in the study of complex photochemical reaction dynamics⁴, where the preparation⁵, evolution⁶ and relaxation of vibrational wavepackets far from equilibrium⁷ can be tracked by using a direct analysis of the X-ray signals in time. The experiments have a sensitivity that is similar to MeV ultrafast electron diffraction^{8,9}. Extensive theoretical studies have been also made in order to formulate a unified X-ray scattering theory^{10–12} with a special attention to the time-resolved picture in atomic^{13–16} and molecular systems^{17–19}.

Even though the theoretical formulation of time-resolved X-ray scattering has provided most of the tools to analyse nuclear^{11,20,21} and electron dynamics^{22–24} in X-ray experiments, the manifestation of these effects, in particular with regards to electron dynamics in excited polyatomic systems^{25–27} remains a very active research area. The slow evolution of the nuclear degrees of freedom and the fast electron rearrangement in these systems require a compromise between resolution and sensitivity in the X-ray scattering signal measurement, as well as accurate theoretical simulations to interpret the experimental results. It has been recently demonstrated theoretically that X-ray scattering for electron dynamics is primarily sensitive to the time-derivative of the density, rather than the instantaneous density^{17–19} and electronic currents can be reconstructed from instantaneous resonant X-ray scattering signals²⁸. That is, considering only the electron dynamics on an attosecond time scale, the dynamical information is primarily contained in the inelastic parts of the scattering while the elastic part remains unchanged. This arises from the coupling of the X-ray probe with the time-evolving system where only the coherent-mixed terms between different electronic states contribute²⁴. In a more intuitive physical picture, since this derivative is proportional to the divergence of the electron currents, time-resolved X-ray scattering can be viewed as a probe of the curvature and magnitude of the electron flow in the system. The instantaneous electron density, on the other hand, appears only as a background. As a result, molecules that support divergent curved electron currents are likely to be convenient for X-ray scattering studies.

^a Department of Chemistry, Brown University, Providence, Rhode Island 02912, USA.

^b Department of Chemistry, 232 Choppin Hall, Baton Rouge, Louisiana 70803, USA

^c EaStCHEM, School of Chemistry, University of Edinburgh, David Brewster Road, EH9 3FJ Edinburgh, United Kingdom.

^d Center for Computation and Technology, Louisiana State University, Baton Rouge, Louisiana 70803, USA

Conjugated, ring-shaped molecules are intriguing candidates for scattering studies of electron dynamics, as recently demonstrated by Hermann *et al.*¹⁹ and Bredtmann *et al.*²⁹, since their driven electron density travels in semi-circular currents that have appreciable divergence^{30,31}. Additionally, they have been used extensively as targets for electron and X-ray scattering^{2,6,32–34}, and are readily functionalized with heteroatoms that allow for site-selective X-ray ionization^{35–37}. The presence of heteroatomic centers, for example, can also lead to long-lived vibrational coherence preservation³⁸. Additionally, ring molecules are ubiquitous in chemistry and form the basis for a wide range of applications including drug design^{39,40}, agrochemistry^{41,42}, material science^{43,44}, and electronics^{45,46}. They also undergo ring-opening and similar processes, which are the subjects of intense interest due to their importance in general organic synthesis⁴⁷, synthesis of photobiological compounds^{48,49} or production of new materials⁵⁰. The role of electron dynamics in these processes, however, remains relatively unstudied. Elucidating them is critical as they may, for example, affect the ring-opening and fragmentation pathways by dictating which bonds break during the reaction. Due to the complexity of the scattering signals, simulations are necessary for the interpretation of the resulting scattering patterns.

In this paper we present a detailed study of how gas-phase X-ray scattering can map stationary core-holes and core-hole-induced dynamics in the oxazole molecules. Oxazole is a five-membered ring molecule containing oxygen, nitrogen and three carbon atoms in different chemical environments that plays an important role in the synthesis of potential medicines including antitumor, antimicrobial, anti-infective, cardiovascular, and nervous system agents⁵¹. It can also undergo photoinduced ring-opening reactions, and is well-studied by theoretical simulations^{52–54} and time-resolved photoelectron spectroscopy⁵². We show how the a K-edge core-hole on each of the centers influences the elastic and inelastic components^{55,56} of the scattering signal, which sheds light on which site is most suitable for initializing and mapping electron/nuclear dynamics. Additionally, we study the electron dynamics triggered by a oxygen core-hole, and demonstrate how the resulting ring currents can be probed by X-ray scattering. These proof-of-principle results aim to lay the foundation for future experiments probing both the electronic and nuclear degrees of freedom using X-ray ionization followed by X-ray scattering.

2 Theory

To simulate the core-hole processes and resulting scattering patterns, we use density functional theory (DFT) to construct a stationary core-hole, real-time time-dependent DFT to simulate the electron density evolution following ionization, and stationary and time-resolved X-ray scattering theories to generate the scattering signals. These methods are briefly described below.

2.1 X-ray scattering from a time-evolving electron density

In the context of a fixed-nuclei approximation and a detection window $\Delta\omega$ larger than the electronic transition energies of the

molecule, the time-dependent differential scattering cross-section reads^{24,57},

$$\frac{d\sigma}{d\Omega} = \left(\frac{d\sigma}{d\Omega} \right)_{\text{Th}} W(\Delta\omega) \int I(t) \langle \Psi(\mathbf{r}^N, t) | \hat{L}(\mathbf{q}, \mathbf{r}^N)^\dagger \hat{L}(\mathbf{q}, \mathbf{r}^N) | \Psi(\mathbf{r}^N, t) \rangle dt, \quad (1)$$

where $\left(\frac{d\sigma}{d\Omega} \right)_{\text{Th}}$ is the Thomson differential cross-section, $W(\Delta\omega)$ is the window function independent of the rovibrational energies that can be approximated as $W(\Delta\omega) \approx 1$, $I(t)$ is the probe-pulse intensity, $\Psi(\mathbf{r}^N, t)$ is the field-free wavepacket, $\hat{L}(\mathbf{q}, \mathbf{r}^N)$ the scattering operator defined as $L(\mathbf{q}, \mathbf{r}^N) = \sum_i^N e^{i\mathbf{q}\mathbf{r}_i}$ where \mathbf{q} is the momentum transfer vector or scattering vector that represents the momentum difference between the incident (\mathbf{k}_0) and scattered (\mathbf{k}_1) beams $\mathbf{q} = \mathbf{k}_1 - \mathbf{k}_0$, N is the number of electrons in the molecule, \mathbf{r} the electron coordinates and t is the time between the pump and probe pulses.

The field-free time evolution of the molecular electronic wavepacket $\Psi(\mathbf{r}^N, t)$ in atomic units can be expressed as,

$$\Psi(\mathbf{r}^N, t) = \sum_j C_j e^{iE_j t} \psi_j(\mathbf{r}^N), \quad (2)$$

where $\psi_j(\mathbf{r}^N)$ are the N -dimensional populated electronic states with E_j eigenenergies and C_j expansion coefficients. Inserting this definition on the expression for the time-resolved differential scattering cross-section in Eq. (1) yields,

$$\begin{aligned} \frac{d\sigma}{d\Omega} = & \left(\frac{d\sigma}{d\Omega} \right)_{\text{Th}} \int I(t) \sum_{ij} C_i C_j \langle \psi_i(\mathbf{r}^N) | \hat{L}^\dagger(\mathbf{q}, \mathbf{r}^N) \hat{L}(\mathbf{q}, \mathbf{r}^N) \\ & \times |\psi_j^*(\mathbf{r}^N) \rangle e^{iE_{ij}t} dt, \end{aligned} \quad (3)$$

with $E_{ij} = E_i - E_j$, which can be solved by either inserting the two-electron scattering operator $\hat{L}^{(2)}(\mathbf{q}, \mathbf{r}_1^N, \mathbf{r}_2^N) = e^{i\mathbf{q}(\mathbf{r}_1^N - \mathbf{r}_2^N)}$, only valid considering the large energy window, or the resolution of the identity in the electronic basis,

$$\hat{1} = \sum_k^\infty |\psi_k(\mathbf{r}^N) \rangle \langle \psi_k(\mathbf{r}^N) |, \quad (4)$$

where k runs over all possible electronic states in the molecule. Combining Eq. (3) and Eq. (4) yields the general form for the expanded differential scattering cross-section¹⁹,

$$\begin{aligned} \frac{d\sigma}{d\Omega} = & \left(\frac{d\sigma}{d\Omega} \right)_{\text{Th}} \int I(t) \left(\sum_{i,k} C_i^2 \left| \int \rho_{ik}(\mathbf{r}) e^{i\mathbf{q}\mathbf{r}} d\mathbf{r} \right|^2 + \right. \\ & \left. + \sum_{i<j,k} 2C_i C_j \int \rho_{ik}(\mathbf{r}) e^{-i\mathbf{q}\mathbf{r}} d\mathbf{r} \int \rho_{kj}(\mathbf{r}) e^{-i\mathbf{q}\mathbf{r}} d\mathbf{r} e^{iE_{ij}t} \right) dt, \end{aligned} \quad (5)$$

where we have introduced the density operator $\hat{\rho}(\mathbf{r}) = \sum_{n=1}^N \delta(\mathbf{r} - \mathbf{r}_n)$ between the electronic states $\psi_i(\mathbf{r}^N)$ to construct the one-electron densities $\rho_{ik}(\mathbf{r}) = \langle \psi_i(\mathbf{r}^N) | \hat{\rho}(\mathbf{r}) | \psi_k(\mathbf{r}^N) \rangle$. The two terms in this expression carry different information about the time dependent X-ray scattering process: the first term corresponds to the time-independent contribution to the signal and acts as a constant background and the second term contains the so-called

coherent-mixed terms^{18,24} which carry the time-dependent information in the X-ray scattering signal.

One can look at the difference between time t and $t = 0$ in Eq. (5) i.e. $\Delta \frac{d\sigma(t)}{d\Omega} = \frac{d\sigma(t)}{d\Omega} - \frac{d\sigma(0)}{d\Omega}$ to trace the time-evolution of the X-ray scattering signal in time,¹⁹

$$\Delta \frac{d\sigma(t)}{d\Omega} = \left(\frac{d\sigma}{d\Omega} \right)_{\text{Th}} \int I(t) \left(\sum_{i<j,k} -4C_i C_j \mathcal{F}[\rho_{ik}(\mathbf{r})] \mathcal{F}[\rho_{kj}(\mathbf{r})] \sin^2 \left(\frac{E_{ij}t}{2} \right) + 2C_i C_j \mathcal{F}[\rho_{ik}(\mathbf{r})] \mathcal{F}[\rho_{kj}(\mathbf{r})] i \sin(E_{ij}t) \right) dt, \quad (6)$$

where $\mathcal{F}[\rho(\mathbf{r})]$ is the Fourier transformation of the electron density. The coupled Fourier transformations can be further simplified by including the double Fourier transformation of the two-electron reduced density matrix $\Gamma(\mathbf{r}_1, \mathbf{r}_2)$,

$$\Delta \frac{d\sigma(t)}{d\Omega} = \left(\frac{d\sigma}{d\Omega} \right)_{\text{Th}} \int I(t) \left(\sum_{i<j} -4C_i C_j (\mathcal{F}^{(2)}[\Gamma_{ij}(\mathbf{r}_1, \mathbf{r}_2)]) \sin^2 \left(\frac{E_{ij}t}{2} \right) + 2C_i C_j (\mathcal{F}^{(2)}[\Gamma_{ij}(\mathbf{r}_1, \mathbf{r}_2)]) i \sin(E_{ij}t) \right) dt, \quad (7)$$

with,

$$\mathcal{F}^{(2)}[\Gamma_{ij}(\mathbf{r}_1, \mathbf{r}_2)] = N + \iint \Gamma_{ij}(\mathbf{r}_1, \mathbf{r}_2) e^{i(\mathbf{r}_1 - \mathbf{r}_2) \cdot \mathbf{q}} d\mathbf{r}_1 d\mathbf{r}_2, \quad (8)$$

where N is the number of electrons in the molecule, as before.

Each term in Eq. (7) represents a different component of the scattering signal. The first term, expected to be small¹⁹, is related to the time evolution of the one-electron density $\Delta\rho(\mathbf{r}, t)$,

$$\Delta\rho(\mathbf{r}, t) = -4 \sum_{i<j} C_i C_j \rho_{ij}(\mathbf{r}) \sin^2 \left(\frac{E_{ij}t}{2} \right). \quad (9)$$

As an ansatz, we relate the second term to the the time derivative of the electron-density in Eq. (26),

$$\frac{d\rho(\mathbf{Q}, t)}{dt} = 2 \sum_{i<j} C_i C_j \mathcal{F}[\rho_{ij}^N(\mathbf{r})] \sin(E_{ij}t). \quad (10)$$

This relationship has been qualitatively demonstrated for a two-level superposition.¹⁹ The density time-derivative is related to the electron-flux in the molecule (Eq. (29)) through the continuity relation in real-space,

$$\frac{d\rho(\mathbf{r}, t)}{dt} = -\nabla \cdot \mathbf{j}(\mathbf{r}, t). \quad (11)$$

2.2 X-ray scattering from a stationary state

The time-independent double differential cross section for X-ray scattering using Eq. (3) is⁵⁸,

$$\frac{d\sigma}{d\Omega d\omega'} = \left(\frac{d\sigma}{d\Omega} \right)_{\text{Th}} S(\mathbf{q}, \omega'), \quad (12)$$

where $\omega' = \omega_0 - \omega_1$, expressing the difference of energy between the incoming and scattered x-rays. The dynamic structure factor $S(\mathbf{q}, \omega')$ is the key value in this equation as it describes the material response. It is given by,

$$S(\mathbf{q}, \omega') = \sum_k \left| \langle \psi_k(\mathbf{r}^N) | \hat{\rho}(\mathbf{r}) | \psi_0(\mathbf{r}^N) \rangle e^{-i\mathbf{q}\mathbf{r}} \right|^2 \delta(E_k - E_0 - \hbar\omega') \quad (13)$$

where $|\psi_k(\mathbf{r}^N)\rangle$ and $|\psi_0(\mathbf{r}^N)\rangle$ are the final and initial electronic states with energies E_k and E_0 respectively. The transition energy $\hbar\omega' = E_k - E_0$, is often negligible compared to the energy of hard x-rays⁵⁹. Therefore, $S(\mathbf{q}, \omega')$ in Eq. (13) can be rewritten as $S(\mathbf{q})$ after the integration over ω' . $S(\mathbf{q})$ can be expressed as the Fourier transform of the reduced two-electron density matrix $\Gamma(\mathbf{r}_1, \mathbf{r}_2)$, which yields,

$$S(\mathbf{q}) = \iint \Gamma(\mathbf{r}_1, \mathbf{r}_2) e^{i\mathbf{q}(\mathbf{r}_1 - \mathbf{r}_2)} d\mathbf{r}_1 d\mathbf{r}_2 + N, \quad (14)$$

with N as the number of electrons in the molecule. From this equation, it can be noticed that total scattering is a combination of one and two-electron terms and electron correlation has a key importance in its calculation^{60,61}. The total scattering signal can be further decomposed by considering only the diagonal terms in Eq. (13) i.e. $\langle \psi_0 | \hat{\rho}(\mathbf{r}) | \psi_0 \rangle e^{-i\mathbf{q}\mathbf{r}}$, giving rise to the elastic component of X-ray scattering. This corresponds to the Fourier transform of the electron density,

$$S_{\text{el}}(\mathbf{q}) = \left| \langle \psi_0 | \hat{\rho}(\mathbf{r}) | \psi_0 \rangle e^{i\mathbf{q}\mathbf{r}} \right|^2 = \left| \int \rho_{00}^{(N)}(\mathbf{r}) e^{i\mathbf{q}\mathbf{r}} d\mathbf{r} \right|^2. \quad (15)$$

Here, $S_{\text{el}}(\mathbf{q})$ is known as the elastic structure factor and $\rho_{00}^{(N)}(\mathbf{r})$ is the one-electron density of the stationary electronic state. The total *inelastic* scattering, $S_{\text{inel}}(\mathbf{q})$, is usually defined as the difference between the total scattering and the *elastic* scattering, i.e.

$$S_{\text{inel}}(\mathbf{q}) = S(\mathbf{q}) - S_{\text{el}}(\mathbf{q}). \quad (16)$$

The limits for the elastic and inelastic components with respect to the amplitude of the momentum transfer vector, $q = |\mathbf{q}|$, are $S_{\text{el}}(0) = N^2$, $S_{\text{inel}}(\infty) = N$ and $S_{\text{el}}(\infty) = S_{\text{inel}}(0) = 0$, which is calculated from Eq. (20) and Eq. (30) where N is the number of electrons in the system. Several methods exist to calculate the total $S(\mathbf{q})$, elastic $S_{\text{el}}(\mathbf{q})$ and inelastic cross-sections $S_{\text{inel}}(\mathbf{q})$. Some of them use the analytical properties of the Gaussian type orbitals (GTOs) based wavefunctions^{55,56,62,63} and others draw upon the numerical Fourier transformation of the reduced one- and two-electron density matrices⁶⁴.

2.3 Real-time time dependent functional theory

Real-time first principles approaches^{65,66}, including TDCI^{67,68}, TD-CASSCF⁶⁹ and TDCC⁷⁰ etc., are natural for capturing non-perturbative electron motion by solving the Schrödinger equation in time. As an extension of DFT, RT-TDDFT⁷¹⁻⁷⁴, which has been shown previously to give good agreement with methods such as ADC(2)⁷⁵, offers a good balance between efficiency and accuracy by propagating the non-interacting one-electron density (or N one-body functions), instead of the N -body wavefunction. In a

Kohn-Sham (KS) framework this is given by,

$$i\frac{\partial}{\partial t}\varphi_i(\mathbf{r},t) = \left\{ -\frac{1}{2}\nabla^2 + v_{\text{ext}}[\rho](\mathbf{r},t) + v_H(\mathbf{r},t) + v_{\text{xc}}[\rho](\mathbf{r},t) \right\} \varphi_i(\mathbf{r},t), \quad (17)$$

where the electron-nuclear and electron-perturbation interactions are described by $v_{\text{ext}}(\mathbf{r},t)$, $v_H(\mathbf{r},t)$ gives the mean-field electron-electron interaction and $v_{\text{xc}}[\rho](\mathbf{r})$ is the exchange correlation potential, for which we use the adiabatic (local in time) approximation. Here the i^{th} KS orbital φ_i is described by a Slater determinant, and the one-particle density $\rho(\mathbf{r},t)$ is given by,

$$\rho(\mathbf{r},t) = \sum_i^{\text{occ}} |\varphi_i(\mathbf{r},t)|^2. \quad (18)$$

In principle, RT-TDDFT can account for the dynamics exactly but in practice the exchange correlation functions have to be approximated. Due to the adiabatic approximation typically made to the functionals, RT-TDDFT can be problematic for resonant excitation processes^{76,77}, and the results may depend on the preparation of the initial state. Another error that arises from approximate functionals is the unphysical self-energy and the incorrect asymptotic potential. Besides turning to self-interaction correction (SIC)^{78,79}, hybrid functionals (such as B3LYP, PBE0 etc.) can also reduce this error to some extent. Since delocalized valence density motion dominates the dynamics after the core-electron is ionized^{75,80,81}, hybrids are well-suited to study these processes.

RT-TDDFT with Gaussian basis sets is especially popular in theoretical chemistry and been applied to the study of strong field ionization^{82,83}, whole energy range excitations⁸⁴⁻⁸⁷ and transient spectroscopy^{88,89} among others. Using a basis of n Gaussian functions as atomic orbitals (AOs) $\{\chi_\mu\}$, the molecular orbitals (MOs) can be written as the linear combination of AOs,

$$\varphi_i(\mathbf{r},t) = \sum_\mu^n A_{\mu i}(t)\chi_\mu(\mathbf{r}), \quad (19)$$

and thus, $\rho(\mathbf{r},t)$ can be computed as

$$\rho(\mathbf{r},t) = \sum_{\mu\nu}^n \mathbf{P}_{\mu\nu}(t)\chi_\mu(\mathbf{r})\chi_\nu^*(\mathbf{r}), \quad (20)$$

with the density matrix \mathbf{P} is calculated as the projection of density to the AOs,

$$\mathbf{P}_{\mu\nu}(t) = \sum_i^n \mathbf{A}_{\mu i}(t)\mathbf{A}_{\nu i}^*(t), \quad (21)$$

and the density matrix in the basis of molecular orbitals (Kohn-Sham eigenstates) \mathbf{P}^{MO} can be calculated by projecting density matrix in AOs with the coefficient matrix \mathbf{A} (for simplicity here assumes no linear dependency occurs),

$$\mathbf{P}^{\text{MO}} = \mathbf{A}^\dagger \mathbf{P} \mathbf{A}, \quad (22)$$

where \mathbf{P}^{MO} is a diagonal matrix in ground state.

With the prepared initial states, the density matrix can be propagated via von Neumann equation, which is typically done in the canonical basis (denoted with prime notation). In the basis of

canonical orbitals, the density matrix propagated is given by,

$$\frac{\partial \mathbf{P}'(t)}{\partial t} = -i[\mathbf{F}'(t), \mathbf{P}'(t)], \quad (23)$$

where the \mathbf{P}' and \mathbf{F}' are the density and Fock matrix in the CO basis. These are obtained by a projecting the density matrix in to the orthogonal basis set COs. The details of the procedure of transforming between basis sets representations can be found in Ref. 90. The time-dependent matrix can be calculated by integrating Eq. 23 over time with a second order Magnus propagator:

$$\mathbf{P}'(t + \Delta t) = e^{\Omega} \mathbf{P}'(t) e^{-\Omega}, \quad (24)$$

$$\Omega = -i\mathbf{F}'(t + \frac{\Delta t}{2})\Delta t. \quad (25)$$

The time-derivative of the density is most conveniently computed in the AO basis,

$$\frac{d\rho(\mathbf{r},t)}{dt} = \sum_i^n \sum_{\mu\nu}^n \frac{d\mathbf{P}_{\mu\nu}(t)}{dt} \chi_{\mu i}(\mathbf{r})\chi_{\nu i}^*(\mathbf{r}), \quad (26)$$

The reciprocal space representation, $\frac{d\rho(\mathbf{Q},t)}{dt}$, which is an important quantity for computing the X-ray scattering signals, can be calculated by a three-dimensional Fourier transformation of the time-derivative of the density matrix in the previous equation,

$$\frac{d\rho(\mathbf{Q},t)}{dt} = \int_{-\infty}^{\infty} \frac{d\rho(\mathbf{r},t)}{dt} e^{-2\pi i \mathbf{Q} \cdot \mathbf{r}} d\mathbf{r}. \quad (27)$$

Besides directly looking into the density change in space, the electronic current density $\mathbf{j}(\mathbf{r},t)$ is a key quantity for interpreting the dynamics, since the scattering is related to its divergence Eqs. (10 and 11). It is defined as,

$$\mathbf{j}(\mathbf{r},t) = \sum_i^n -\frac{i}{2} (\varphi_i^* \nabla \varphi_i - \varphi_i \nabla \varphi_i^*), \quad (28)$$

and can be calculated in the AO basis using the density matrix $\mathbf{P}(t)$:

$$\mathbf{j}(\mathbf{r},t) = -\frac{i}{2} \sum_{\mu\nu}^n [\mathbf{P}(t)_{\nu\mu} \lambda_\mu^* \nabla \chi_\nu - \mathbf{P}(t)_{\mu\nu} \chi_\mu \nabla \lambda_\nu^*]. \quad (29)$$

The AO gradients Eq. (29) are typically available in any electronic structure code.

2.4 Calculation of scattering matrix elements from a core-hole

As the core-hole initial state considered here is non-stationary, \mathbf{P}^{MO} becomes non-diagonal and the transition amplitude between different states come into the off-diagonal elements. However, a diagonalized core-hole matrix $\mathbf{P}_+^{\text{MO, diag}}$ can be obtained by projecting the non-stationary density \mathbf{P}_+ to the neutral ground state:

$$\mathbf{P}_+^{\text{MO, diag}} = \mathbf{A}_0^\dagger \mathbf{P}_+ \mathbf{A}_0. \quad (30)$$

In the context of a DFT/RT-DDFT derivation as the one presented in Sec. 2.3, molecular electronic wavefunctions can be

constructed as a linear combination of Slater orbitals,

$$|\psi\rangle = \sum_{i=1}^{N_{\text{conf}}} c_i |\phi_{\text{SD}}^i\rangle, \quad (31)$$

where the c_i are the configuration interaction coefficients, N_{conf} is the number of configurations included in the expansion, and $|\phi_{\text{SD}}^i\rangle$ are the Slater determinants. In the case of a single determinant method such as DFT, the wavefunction is built using a single Slater determinant and $c_1 = 1$. Each Slater determinant in Eq. (31) is constructed as a sum of spin-orbitals, $\varphi_i(\mathbf{r})$, where \mathbf{r} are the electron coordinates. The expansion of the one-electron density matrix in Eq. (18) using these spin-orbitals can be then inserted in Eq. (15) to obtain the elastic structure factor S_{el} ,

$$S_{\text{el}}(\mathbf{q}) = \left| \int \sum_{l,m}^{\text{occ}} \varphi_l(\mathbf{r}) \varphi_m(\mathbf{r}) e^{i\mathbf{q}\cdot\mathbf{r}} d\mathbf{r} \right|^2. \quad (32)$$

For single-reference methods, the two-particle density matrix elements Γ_{klmn} can be constructed from the diagonal (stationary) one-particle density matrix elements P_{kl} (Eq. (30)) that are equal to the occupation number of the molecular orbitals,

$$\Gamma_{klmn}^{ij} = P_{mk}^i P_{ln}^j - P_{ml}^i P_{nk}^j \quad (33)$$

where i and j correspond to the two electronic states considered. The reduced two-electron density matrix then reads,

$$\Gamma_{ij}^{(2)}(\mathbf{r}_1, \mathbf{r}_2) = \sum_{klmn}^{N_{\text{orb}}} \Gamma_{klmn}^{ij} \varphi_k^i(\mathbf{r}_1) \varphi_l^i(\mathbf{r}_1) \varphi_m^j(\mathbf{r}_2) \varphi_n^j(\mathbf{r}_2), \quad (34)$$

where γ_{klmn}^{ij} are the two-electron reduced density matrix elements if $i = j$, and the two-electron reduced transition matrix elements when $i \neq j$ obtained through Eq. (33). N_{orb} is the number of occupied spin-orbitals $\varphi_i^i(\mathbf{r})$ forming every Slater determinant, $|\Phi_{\text{SD}}^i\rangle$. Combining Eq. (14) with the definition of the two-electron density matrix, the expression for the total X-ray scattering dynamic factor reads

$$S(\mathbf{q}) = \iint \sum_{klmn}^{N_{\text{orb}}} \gamma_{klmn}^{ij} \quad (35)$$

$$\varphi_k^i(\mathbf{r}_1) \varphi_l^i(\mathbf{r}_1) \varphi_m^j(\mathbf{r}_2) \varphi_n^j(\mathbf{r}_2) e^{i\mathbf{q}\cdot(\mathbf{r}_1 - \mathbf{r}_2)} d\mathbf{r}_1 d\mathbf{r}_2 + N,$$

which leads to the resolution of two coupled integrals in \mathbf{r}_1 and \mathbf{r}_2 . Eqs. (32 and 35) can be solved analytically, as demonstrated in Wang and Smith⁹¹ and Zotev *et al.*⁶³.

3 Results

In this section we demonstrate how X-ray scattering can be used to measure the existence of stationary-state core-holes in molecules with multiple heteroatoms (Section 3.1), as well as attosecond electron dynamics following rapid core-hole ionization (Section 3.2). As a model system we use oxazole, a quasi-planar hetero-aromatic molecule. Since the dynamics we study are faster than the life time of an oxygen K-edge core-hole (~ 9 fs)⁹², we do not take the Auger decay into account. All electronic structure calculations used the density functional theory (DFT) and RT-TDDFT

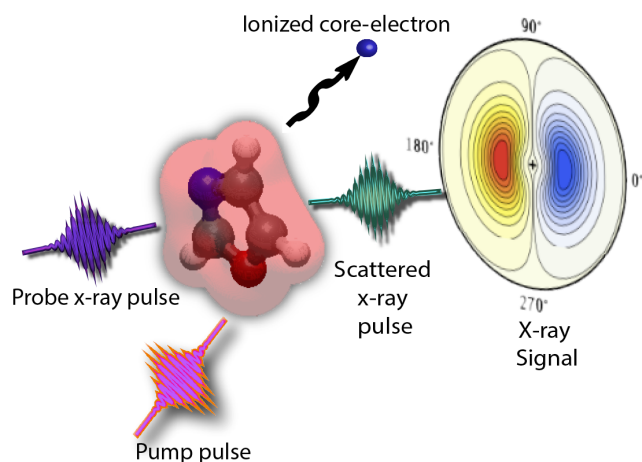


Fig. 1 Schematic representation of the inner-shell ionization in oxazole and subsequent probing by an X-ray pulse.

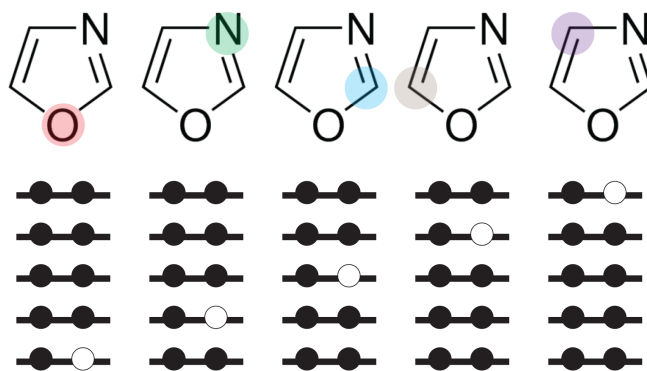


Fig. 2 Schematic representation of the oxazole molecule core-hole ionization. The upper row highlights the atom in oxazole in which ionization occurs and the bottom row illustrates the molecular orbitals (MOs) affected by this ionization with the vacancies represented as empty circles. The MOs represented in this figure only constitute the five lowest-lying molecular orbitals in oxazole.

module⁷¹ in NWChem⁹³. The gas-phase geometry was optimized using DFT with the B3LYP functional and cc-pvdz basis. All density matrices (stationary or time-dependent) used for computing the stationary scattering were also generated using this basis and geometry.

3.1 Stationary X-ray scattering after selective core-hole ionization in oxazole

We investigate how X-ray scattering can map the selective inner-shell ionization of oxazole and explore the effect of the electron loss on the total ($S(\mathbf{q})$), elastic ($S_{\text{el}}(\mathbf{q})$) and inelastic ($S_{\text{inel}}(\mathbf{q})$) scattering signals using stationary electronic states. The process studied is represented schematically in Fig. 1.

The DFT ground neutral state was converged with optimized

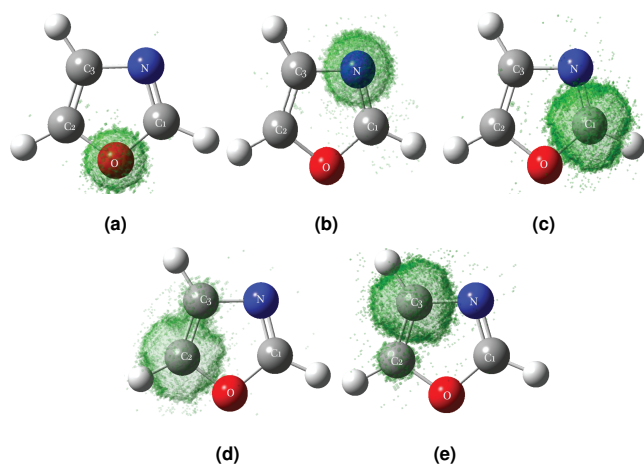


Fig. 3 The one-electron density difference isosurfaces for the five stationary K-edge core-hole ionizations considered in oxazole. Each subfigure shows the difference between the neutral ground-state density and the ionized stationary density $\Delta\rho(\mathbf{r}) = \rho_0(\mathbf{r}) - \rho_+(\mathbf{r})$ for a) O, b) N, c) C₁, d) C₂, and e) C₃. All plots have an isosurface value of 10^{-6} a.u.³.

molecular geometry, then the initial K-edge core-hole states were created by removing a core electron from the corresponding Ks ground state orbital. Next, the total, elastic and inelastic contributions to the X-ray scattering signals were calculated using the methods outlined in the theory section (Eqs. (14, 16 and 15) and our own codes^{55,56,63,94}. The one-electron density matrices were diagonalized in the neutral ground-state basis using Eq. (30) and the two-electron density matrices were constructed (Eq. (34)) from the one-electron ones following the convention for single-reference wavefunctions and maintaining the N-representability conditions⁹⁵.

To determine the effect of a stationary core-hole on the scattering, five different core-holes were created in the oxazole molecule (O, N, C₁, C₂, C₃), each corresponding to a relaxed K-edge core-hole in a different atom in the molecule. The different chemical environments of these atoms give rise to five different non-bonding core orbitals that can be ionized with a high-energy photon (see Fig. 2). The ionization of different atomic centers is predicted to result in distortions in the one- and two-electron densities that can be mapped using the stationary X-ray scattering expressions presented in the theory section (Eqs. (14,15 and 16)). Fig. 3 shows the effect of the core-hole ionizations on the oxazole one-electron density. Each subfigure represents the difference between the ionized and the neutral ground state one-electron densities $\Delta\rho(\mathbf{r}) = \rho_0(\mathbf{r}) - \rho_+(\mathbf{r})$. All show a spherical shape corresponding to the ionization from a s-shaped molecular orbital. The ionization of the K-edge in O is the most compact and localized (Fig. 3a), followed by the N K-edge and the three C core orbitals. The core orbitals in the three carbon atoms are quasi-degenerate, thus the core-hole ionization produce analogous one-electron differences in the three of them, with small differences arising from the different atomic surroundings. In practice, using a photon pulse with any appreciable bandwidth would render these three carbon atoms indistinguishable, but we report all three values here for completeness.

Fig. 4 shows the calculated percent total, elastic and inelastic differences for the five inner-shell ionizations considered in oxazole. The X-ray wavelength is chosen as $\lambda = 1.26$ Å (energy of 9.7 keV) corresponding to a momentum space of $(0, 10$ Å⁻¹), which is the maximum range conceivable for a 9.7 keV X-ray photon energy. The percent differences have been calculated using the signal from the ionized species $S_+^x(q)$ and the neutral ground-state molecular signals $S_0^x(q)$ as the reference, where x represents the total, elastic and inelastic structure factors as defined in Eqs. (14, 15 and 16) respectively,

$$\Delta\%I_x(q) = 100 \frac{(S_+^x(q) - S_0^x(q))}{S_0^x(q)}. \quad (36)$$

All the values in Fig. 4 are rotationally averaged X-ray scattering signals, *i.e.*, all changes in the one- and two-electron density matrices of the molecule as a consequence of core-hole ionization have been spatially averaged over all possible molecular orientations.

Looking at the total percent differences in Fig. 4a, one can see that all ionization signals show a common behaviour at $q = 0$ and $q \approx \infty$, with a depletion in the signal of -5.5% and -2.7% respectively. This is a result of the electron loss experienced by the molecule in the ionization process *i.e.* $(N_+^2 - N_0^2)/N_0^2 = (35^2 - 36^2)/36^2 \times 100 = -5.5\%$ for $q = 0$ and $(N_+ - N_0)/N_0 = (35 - 36)/36 \times 100 = -2.8\%$ for $q \approx \infty$, where N_+ and N_0 are the number of electrons in the cation and the neutral molecules respectively. It is noteworthy that the ionization in the oxygen K-edge (red line) produces the most noticeable change in the total X-ray signal, with a signal decay of approximately 10% between $q = 4$ and $q = 6$ Å⁻¹.

This change in the total signal is related to the position and shape of the core-hole created in the molecule when the oxygen K-edge orbital is ionized (see Fig. 3a). The highly localized real-space difference density around the oxygen atom makes the change appear at larger values of q and with a larger incidence. Furthermore, K-edge ionization of the oxygen and nitrogen atoms reduces the X-ray signal more than in the case of carbon atoms (Figs. 4a and 4b). This is likewise a consequence of the more spatially diffuse carbon core-holes, where the density is redistributed among the neighboring atoms to a larger extent (see Figs. 3c,d,e).

It is important to note that the total X-ray scattering differences not only map a change in the one-electron properties of the molecule but also the correlation between their electrons, including both the elastic and the inelastic contributions of the X-ray scattering signal. The elastic signals in Fig. 4b show the same trend as the total X-ray scattering differences, albeit with much bigger maximum percent difference values, reaching up to -20% . As the elastic signal is calculated as the Fourier transformation of the one-electron molecular density, the two-electron terms included in the total X-ray scattering signal are not considered and the difference increases. The vanishing values of the elastic X-ray signals at large values of q also increase these percent differences as the denominator in Eq. (36) is very small. The differences between elastic and inelastic signals can be explained by considering the nature of the X-ray scattering processes involved. While

elastic X-ray scattering only maps the one-electron density in the molecule, the inelastic X-ray scattering signal considers all possible transitions between the occupied and virtual electronic states. The probability of these transitions is inversely proportional to the energy difference between the levels considered⁵⁶. Accordingly, the ejection of one core-electron from the molecule does not produce a very significant change in the inelastic scattering signal and the trend shown in the total and elastic signals is inverted; The core-hole in the C atoms produces a larger difference than in N and O. The three C K-edges are quasi-degenerate, hence the three inelastic X-ray scattering signals are almost identical (see Fig. 4c).

Fig. 4d shows the q -integrated percent difference, $\int_{q_{min}}^{q_{max}} |\% \Delta I(q)| dq$. This demonstrates the overall effect of the different ionizations in the scattering signals (total, elastic and inelastic). We can see that the trend is the same for total and elastic representations, with the O K-edge ionization producing the largest difference, followed by N and the three C K-edges. The elastic part of the signal shows much greater differences than the total X-ray scattering. This means that the one electron terms in the signal produce a bigger change than the ones involving two electrons. This is expected, as we are ionizing core electrons that have a small interaction with the rest of electrons in the molecule. Nevertheless, some components of these differences can be introduced by the method used to calculate the percentage. As mentioned before, the big differences in the elastic part could come from its vanishing values at large values of q . The inelastic part, in turn, has an opposite tendency, with the C K-edge ionizations showing the largest difference. The probability of inelastic transitions between the different electronic states in the molecule is inversely proportional to their energy difference and the changes on the inelastic signal respect to the neutral species are small for the more energetic transitions (*i.e.* O and N).

The results presented here show that the core-hole ionization of heteroatomic species, notably O K-edge ionization, produces a significant change in the X-ray scattering signal that could be measured with the state-of-the-art X-ray experimental techniques⁹⁶. The depletion of the signal produced by the ionization process, which has values that sit within the current experimental sensitivity, would allow a fast detection of the sudden electron loss experienced by the molecular system and reveal further insights about the nature of this process. The core energy and density localization both play roles in the scattering process, as the more localized and energetic core-holes would produce the biggest change in the total scattering signals. The magnitude in the inelastic X-ray scattering changes also suggests that the high energy involved in the core-hole ionization makes the mediated X-ray transitions less probable to happen and thus the largest influence in the X-ray scattering signal change comes from the elastic part.

3.2 Oxygen K-edge core-hole induced attosecond ring currents in oxazole

In this section we show how X-ray scattering may be used to probe coherent attosecond electron dynamics triggered by the inner-

shell ionization. This may be useful, for example for resolving the attosecond electronic density reorganization immediately before nuclear rearrangement in a photochemical reaction. Elucidating this process is critical, as it is predicted to affect the ring-opening and fragmentation pathways, for example, by dictating which bonds break during the reaction. Due to the complexity of the scattering signals, simulations are necessary for interpretation of the resulting scattering patterns. Hermann *et al.*¹⁹ recently demonstrated that the X-ray scattering in this case is primarily sensitive to the rate of change of the density, $\partial_t \rho(\mathbf{r}, t)$, rather than the instantaneous density itself. Drawing on a probability continuity argument ($\partial_t \rho(\mathbf{r}, t) = -\nabla \cdot \mathbf{j}(\mathbf{r}, t)$), attosecond X-ray scattering experiments can thus be viewed as probes of diverging electron currents rather than densities or holes.

As an illustrative example, we study the dynamics induced by rapid core-hole ionization from the O K-edge in the oxazole molecule. We emulate this process by removing an electron from the O 1s orbital, followed by field-free propagation without energy minimization⁷⁵. Removal of an K-edge electron from an atom-like orbital constitutes a reasonable representation of rapid ionization, unlike mixed-state valence cases which are typically multiconfigurational in character^{75,97}. The fast ionization creates a coherent superposition of states which results in density dynamics in the ring. Rapid ionization of this type has been observed to result in charge migration (CM), where a localized hole moves across the molecule^{75,97-101}. For the results presented here, the dynamics are perhaps best thought of as ring currents (continuous density flow) rather than CM. We focus primarily on the relationship between the time-evolving density/flux and the X-ray scattering, however, and do not characterize the dynamics as CM or non-CM. This excitation primarily results in in-plane dynamics along the x -direction (O/N axis), with a negligible evolution in the y and z directions. Following a sudden reorganization near $t \sim 0$, the time-dependent dipole moment along x -axis (O-N direction) oscillates with multiple frequencies due to the effectively broadband nature of the rapid core-hole ionization. The dominant mode has a period of roughly 0.5 fs. In order to determine how these dynamics can be measured using X-ray scattering, we selected five representative snapshots (red dots in Fig. 5) along a half-period. These points correspond to: maximum of the oscillation (a, $t = 0.08$ fs), three intermediate times (b, 0.15 fs; c, 0.21 fs; d, 0.29 fs), and the minimum (e, 0.33 fs). For each of these, the current density $\mathbf{j}(\mathbf{r}, t)$ and the time-derivative of the electron density (in real-space) were computed from the density matrix. Note that the dipole moment and average currents are related to each other but oscillate out-of-phase, *i.e.* the maximum/minimum dipole (points a, e) correspond to times with low average currents, whereas the intermediate times (b,c,d) have significant net currents across the molecule. The absolute value of the momentum-space density derivatives $\left| \frac{d\rho(\mathbf{Q}, t)}{dt} \right|$ was then computed via the absolute value of the 3D FFTs of the real-space $\frac{d\rho(\mathbf{r}, t)}{dt}$. These two quantities, related through the continuity equation in real-space (Eq. (11)), give complimentary information: $\mathbf{j}(\mathbf{r}, t)$ shows the mechanism of electron flow during the process, and $\left| \frac{d\rho(\mathbf{Q}, t)}{dt} \right|$ is related to the time-dependent X-ray

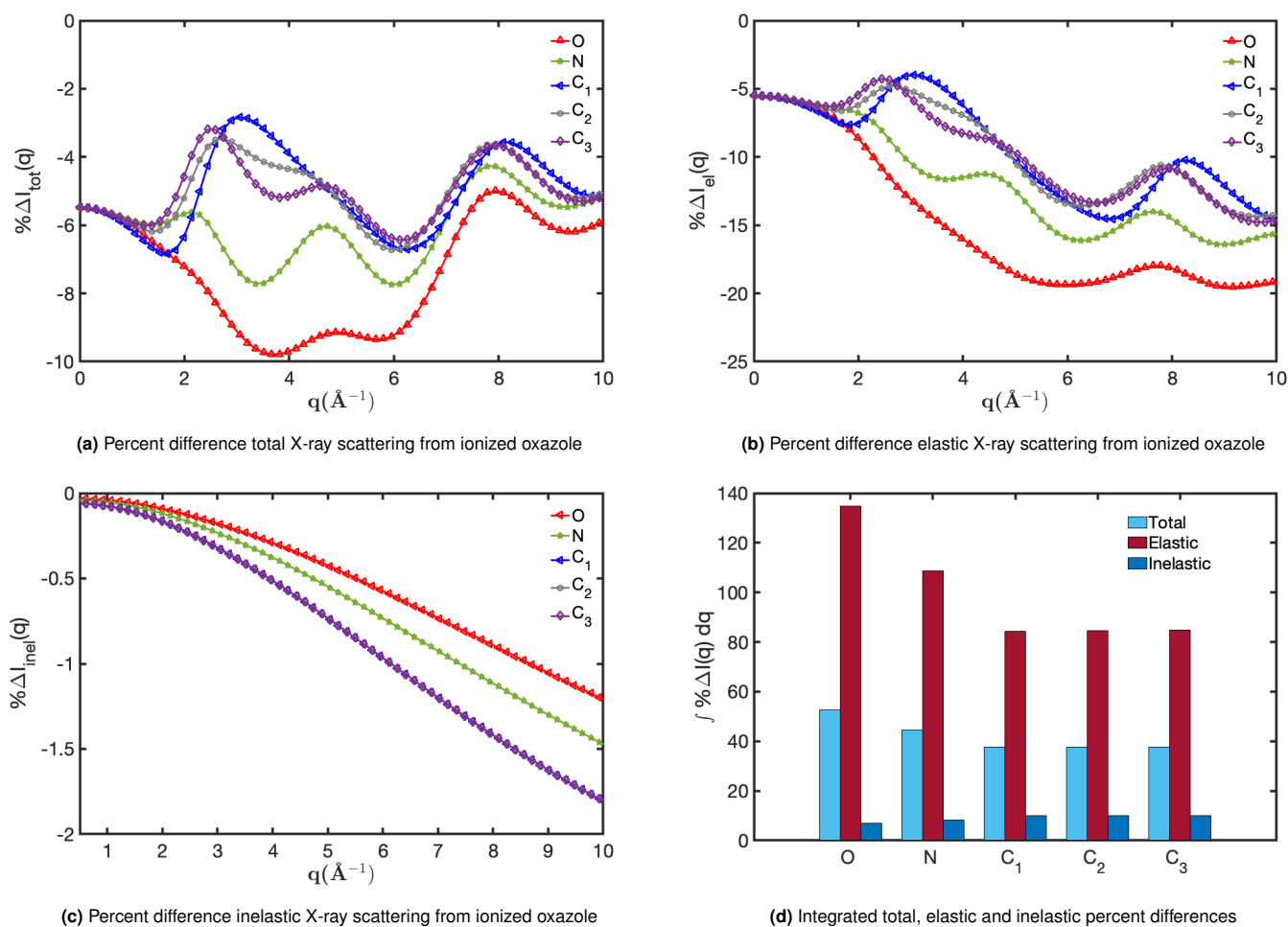


Fig. 4 Calculated percent differences $\Delta\%I(q)$ (Eq. 36) and q -integrated percent differences (see text) for total, elastic and inelastic X-ray scattering signals from the ionized oxazole molecule for an X-ray wavelength of $\lambda = 1.26 \text{ \AA}$. Each line corresponds to a different K-edge ionization represented by the atom under consideration *i.e.*, O (red), N (green), C_1 (blue), C_2 (grey) and C_3 (purple) (see Fig. 2). a) Total X-ray scattering, b) Elastic X-ray scattering, c) Inelastic X-ray scattering, d) Integrated total, elastic and inelastic scattering.

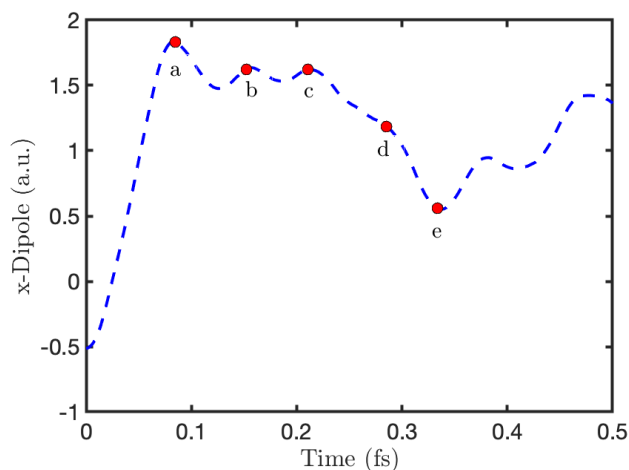


Fig. 5 Computed time-dependent dipole moment of oxazole along X-axis (O-N bond) following an O K-edge core-hole ionization. The five time points chosen for scattering calculations are marked with red circles.

scattering. Finally, to match the conventional experimental conditions we have also included a rotational-averaged representation of the absolute density derivative $\left\langle \left| \frac{d\rho(Q,t)}{dt} \right| \right\rangle_Q$, that accounts for all possible molecular orientations in a random gas-phase ensemble of molecules.

Fig. 6 shows four quantities for the five time snapshots. The top row shows the magnitude of the current densities $\sqrt{\mathbf{j}(\mathbf{r},t) \cdot \mathbf{j}(\mathbf{r},t)}$ 1 Å above the molecular plane. This was chosen to better visualize the currents in the π -conjugated system and avoid showing the strong localized currents flowing to/from each atom, which would appear at Q values beyond the detection limit of current X-ray sources⁹⁶. In this case, the electron density flows across the molecular backbone, resulting in semi-ring currents (discussed below). The second row shows the corresponding current vector lines in this plane. The third row in this figure shows $\left| \frac{d\rho(Q,t)}{dt} \right|$ for the $Q_z = 0 \text{ \AA}^{-1}$ slice of the reciprocal space. This emulates a scattering experiment in which the incident X-ray beam travels in a perpendicular direction with respect to the molecular plane. The momentum-space Q_x and Q_y values range between -15 \AA^{-1} and 15 \AA^{-1} using a 100×100 Q -grid. The localized currents give rise to high Q signals. Due to the direct relationship between $\frac{d\rho(Q,t)}{dt}$ and scattering, these plots are qualitative predictions of the expected X-ray signals at every time point for fixed molecular orientation and rotationally averaged measurements, respectively. As expected, the lack of symmetry in the oxazole molecule results in static patterns that only maintain the centrosymmetry¹⁰². Finally, the fourth row shows the rotationally averaged signal using a 200^2 Q -grid, obtained by integration over the azimuthal and polar angles¹⁰³. The inclusion of rotational averaged values corresponds to a measurement of an ensemble of randomly oriented molecules.

We now discuss the ring-current mechanism in detail and how these currents qualitatively manifest in the scattering patterns. At time 0.08 fs (point a), when the dipole moment reaches its first maximum, there are three distinct current flows: a divergence from the oxygen, and two weak semi-ring counter-currents trav-

eling from the right of the ring towards the oxygen. The diverging currents from the oxygen are localized in space and result in a broad, high Q (starting at $Q = 14 \text{ \AA}^{-1}$) signal that is not fully contained in our reciprocal space representation. These currents are likely related to the rapid response of valence electrons to the core hole created at $t = 0$. The semi-ring currents appear at $Q = 3.1 \text{ \AA}^{-1}$ in momentum space, which is a reflection of the curved electron flow spanning the entire ring. At the second snapshot time (point b, 0.15 fs), the dynamics becomes dominated by two strong right→left semi-ring currents with significant curvature ($C_3 \rightarrow C_2 \rightarrow H$; $N \rightarrow C_1 \rightarrow H$). As the two currents have different curvature and magnitude, this results in two main signals in the scattering at $Q = 2.0 \text{ \AA}^{-1}$ and $Q = 4.5 \text{ \AA}^{-1}$. The broad signal centered at 15 \AA^{-1} remains, but has a lower magnitude. This arises from weak but non-zero converging currents near the oxygen.

At point c (0.21 fs), the currents flow mostly perpendicularly to the direction of the density oscillation (towards $C_2=C_3$ and C_1) with relatively localized linear flows. Since the main two currents have similar magnitudes and curvature, this results in a single broad scattering peak at $Q = 4.2 \text{ \AA}^{-1}$. At the next snapshot (point d; 0.29 fs), the dipole moment in the O-N direction is roughly near the average value and thus expected to have a large current. The current density in Fig. 6 shows a strong left-to-right ring current split into two channels, one from $C_1 \rightarrow C_3$ and another from $C_2 \rightarrow N$. These intersecting currents manifest in the scattering as two distinct peaks at $Q = 3.6 \text{ \AA}^{-1}$ and 6.3 \AA^{-1} . Since the current flows with different curvature (more linear/along the bonds) than in the right-to-left (point b) case, the scattering signals occur at different Q values. As before, the absence of core-hole currents results in no clear peak within the Q range considered. Finally, at 0.33 fs (point e), when the dipole becomes minimum, there are four distinct currents: two converging on O, one diverging from C_1 and one diverging from C_2 . The two ring currents result in a set of low Q peaks at 2.1 \AA^{-1} and 4.2 \AA^{-1} , which is roughly consistent with the positions of the previous ones. Since two of these currents converge sharply on the oxygen core-hole, this results in a strong, broad high Q signal (17.0 \AA^{-1}).

Looking at the results as a whole, there is a clear correlation between the scattering patterns and the currents within the molecule. Broadly speaking, ring currents are mirrored as complex, low Q features, whereas electron flows into/out of a single atom result in a broad, high Q peak. These results also demonstrate that, although the instantaneous density is an important quantity for probing nuclear dynamics, for electron dynamics it is the divergence of the currents (or alternatively the derivative of the density) that dominates the signals.

4 Conclusions

In conclusion, we have presented simulations of the X-ray scattering from stationary core-holes, as well as time-resolved scattering from a system with evolving electron density. For the case of a stationary core-hole, we observe that the difference in the scattering signal between a neutral and ionized oxazole molecule is sufficient for detection with existing experimental sensitivities. Additionally, the more energetic and spatially localized the core-hole,

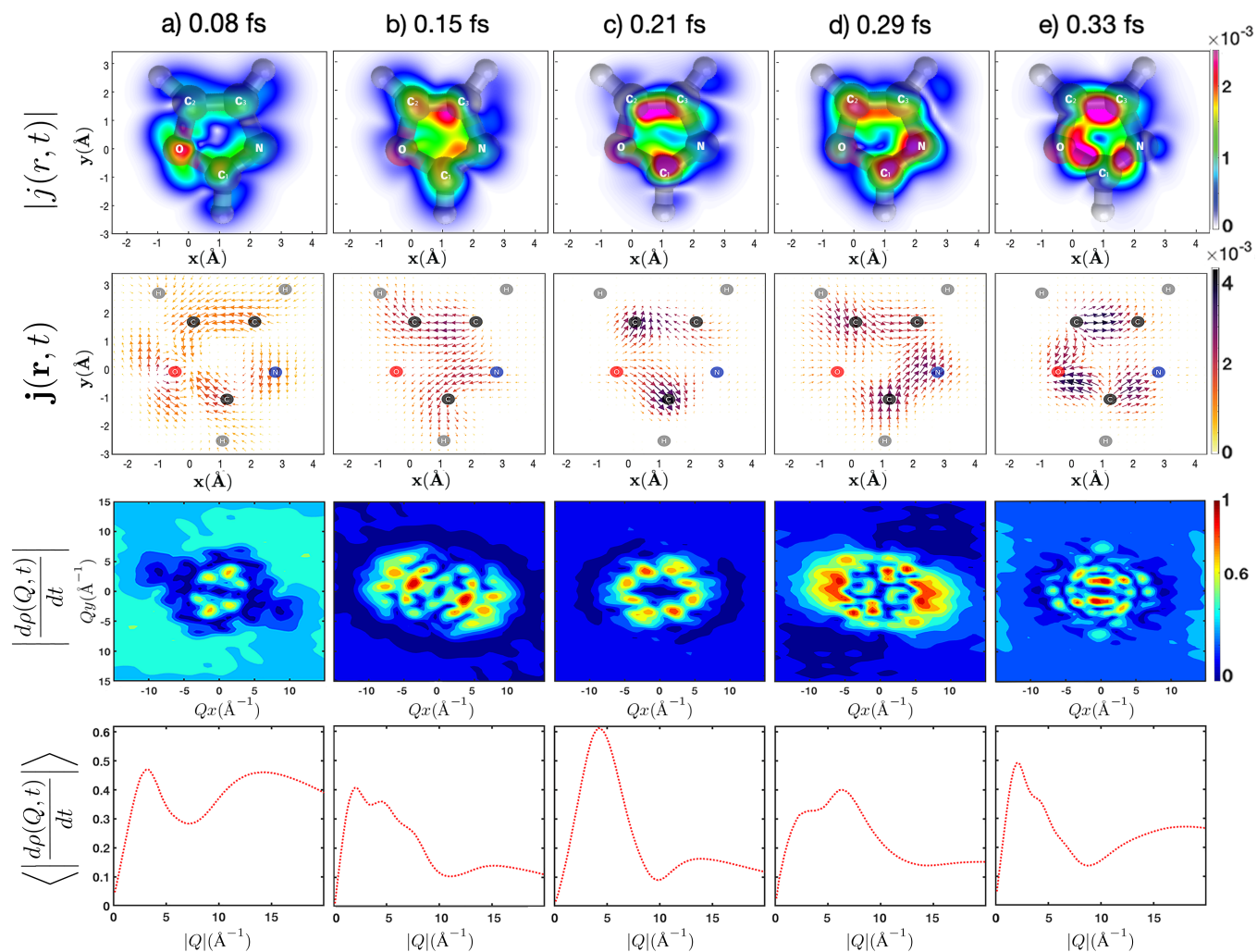


Fig. 6 Simulated electron current magnitude $|j(\mathbf{r}, t)|$ (top row), electron current vector fields $\mathbf{j}(\mathbf{r}, t)$ (second row), absolute value of the Fourier transformed electron density time-derivative $\left| \frac{d\rho(Q, t)}{dt} \right|$ (third row) and rotational-averaged $\left\langle \left| \frac{d\rho(Q, t)}{dt} \right| \right\rangle_{\Omega}$ (bottom row) for five different time delays (columns): 0.08, 0.15, 0.21, 0.29 and 0.33 fs extracted from the dynamics simulation of the O K-edge ionization in oxazole. All the values represented are in a.u. except the distances and momentum vectors which are presented in \AA and \AA^{-1} respectively

the greater the contrast between the signals from the neutral and the ion. For oxazole, an oxygen core-hole results in $\sim 10\%$ maximum decrease while a nitrogen core-hole gives $\sim 8\%$ decrease. These conclusions are important for the design and interpretation of time resolved scattering experiments involving ultrafast electron dynamics. We also observed that the absolute change of the inelastic scattering component was roughly one order of magnitude less than the elastic part, a change that would be even smaller by using the ground-state total signal as the reference. This suggests that when computing scattering from stationary core-holes, the elastic contribution is a good approximation to the total change. Since this only requires a Fourier transform of the density, this greatly simplifies the calculation, and moreover implies that the quality of these scattering calculations might not be significantly improved by inclusion of two-body interactions.

Additionally, we have shown that, at least qualitatively, X-ray scattering can be used to map out the time-dependent electron currents in an excited molecule. In this paper we did not use the analytical scattering expression, and instead related the scattering to the dynamics via the absolute value of the electron density derivative. It is important to note that this gives only a qualitative picture of the mapping between scattering and instantaneous currents. To properly compute this mapping would require either time-dependent two-particle reduced density matrices or explicit calculation of a large number of states in the molecule. Nevertheless, our results capture the essential relationship between electron current and scattering. Here, the instantaneous density is not the quantity that determines the scattering, but instead it is sensitive to the divergence of the electronic currents, as demonstrated by the authors in Ref. 19. As a result, scattering is well-matched to cases where these currents have appreciable curvature, such as in ring-shaped molecules, while maybe less useful for simpler geometries such as linear molecules that have more spatially uniform currents. Rings with heteroatoms are especially promising candidates since the currents can be influenced by the differing electronegativities at the different sites on the ring. For the specific case of an oxygen core-hole ionization in oxazole, we show that the resulting currents that span the ring appear at Q values between 2 and 6 \AA^{-1} , whereas localized currents around into/away from the oxygen atom appear at $Q > 12 \text{ \AA}^{-1}$. This suggests that ring currents can be measured by existing experiments once sufficient time resolution is achieved. This opens the door to measuring the dynamics immediately before ring-opening reactions, where electron ring currents may play an important role in softening the bonds.

5 Acknowledgments

This work was supported by the Department of Energy, Office of Science, Basic Energy Sciences, under award number DE-SC0020276. PMW acknowledges additional support for this research by the National Science Foundation under Award # CHE-1953839.

Notes and references

1 H. Yong, N. Zotev, J. M. Ruddock, B. Stankus, M. Simmermacher, A. M. Carrascosa, W. Du, N. Goff, Y. Chang, D. Bellshaw, M. Liang, S. Carbajo, J. E. Koglin, J. S. Robinson, S. Boutet, M. P. Miniti, A. Kirrander and P. M. Weber, *Nature Communications*, 2020, **11**, 2157.

2 M. P. Miniti, J. M. Budarz, A. Kirrander, J. S. Robinson, D. Ratner, T. J. Lane, D. Zhu, J. M. Glownia, M. Kozina, H. T. Lemke, M. Sikorski, Y. Feng, S. Nelson, K. Saita, B. Stankus, T. Northey, J. B. Hastings and P. M. Weber, *Phys. Rev. Lett.*, 2015, **114**, 255501.

3 J. M. Ruddock, H. Yong, B. Stankus, W. Du, N. Goff, Y. Chang, A. Odate, A. M. Carrascosa, D. Bellshaw, N. Zotev, M. Liang, S. Carbajo, J. Koglin, J. S. Robinson, S. Boutet, A. Kirrander, M. P. Miniti and P. M. Weber, *Science Advances*, 2019, **5**, 1.

4 J. M. Ruddock, N. Zotev, B. Stankus, H.-W. Yong, D. Bellshaw, S. Boutet, T. J. Lane, M. Liang, S. Carbajo, W. Du, A. Kirrander, M. P. Miniti and P. M. Weber, *Angew. Chem. Int. Ed.*, 2019, **58**, 6371–6375.

5 H. Yong, N. Zotev, B. Stankus, J. M. Ruddock, D. Bellshaw, S. Boutet, T. J. Lane, M. Liang, S. Carbajo, J. S. Robinson, W. Du, N. Goff, Y. Chang, J. E. Koglin, M. D. J. Waters, T. I. Sølling, M. P. Miniti, A. Kirrander and P. M. Weber, *J. Phys. Chem. Lett.*, 2018, **9**, 6556–6562.

6 M. P. Miniti, J. M. Budarz, A. Kirrander, J. Robinson, T. J. Lane, D. Ratner, K. Saita, T. Northey, B. Stankus, V. Cofer-Shabica, J. Hastings and P. M. Weber, *Faraday Discuss.*, 2014, **171**, 81.

7 H. Yong, J. M. Ruddock, B. Stankus, L. Ma, W. Du, N. Goff, Y. Chang, N. Zotev, D. Bellshaw, S. Boutet, S. Carbajo, J. E. Koglin, M. Liang, J. S. Robinson, A. Kirrander, M. P. Miniti and P. M. Weber, *J. Chem. Phys.*, 2019, **151**, 084301.

8 M. Stefanou, K. Saita, D. V. Shalashilin and A. Kirrander, *Chem. Phys. Lett.*, 2017, **683**, 300–305.

9 L. Ma, H. Yong, J. D. Geiser, A. Moreno Carrascosa, N. Goff and P. M. Weber, *Structural Dynamics*, 2020, **7**, 034102.

10 R. Santra, *J. Phys. B*, 2009, **42**, 023001.

11 U. Lorenz, K. B. Møller and N. E. Henriksen, *Phys. Rev. A*, 2010, **81**, 023422.

12 K. B. Møller and N. E. Henriksen, *Struct. Bond.*, 2012, **142**, 185.

13 J. Cao and K. R. Wilson, *J. Phys. Chem. A*, 1998, **102**, 9523.

14 S. Bratos, F. Mirloup, R. Vuilleumier and M. Wulff, *J. Chem. Phys.*, 2002, **116**, 10615.

15 G. Dixit, O. Vendrell and R. Santra, *Proc. Natl. Acad. Sci.*, 2012, **109**, 11636.

16 M. Simmermacher, N. E. Henriksen and K. B. Møller, *Phys. Chem. Chem. Phys.*, 2017, **19**, 19740–19749.

17 M. Kowalewski, K. Bennett and S. Mukamel, *Struct. Dyn.*, 2017, **4**, 054101.

18 M. Simmermacher, N. E. Henriksen, K. B. Møller, A. Moreno Carrascosa and A. Kirrander, *Phys. Rev. Lett.*, 2019, **122**, 073003.

19 G. Hermann, V. Pohl, G. Dixit and J. C. Tremblay, *Phys. Rev. Lett.*, 2020, **124**, 013002.

20 C. J. Bardeen, J. Che, K. R. Wilson, V. V. Yakovlev, V. A. Apkarian, C. C. Martens, R. Zadayan, B. Kohler and M. Messina, *J. Chem. Phys.*, 1997, **106**, 8486.

21 U. Lorenz, K. B. Møller and N. E. Henriksen, *New J. Phys.*, 2010, **12**, 113022.

22 G. Dixit and R. Santra, *Phys. Rev. A*, 2017, **96**, 053413.

23 C. Arnold, O. Vendrell and R. Santra, *Phys. Rev. A*, 2017, **95**, 033425.

24 M. Simmermacher, A. Moreno Carrascosa, N. E. Henriksen, K. B. Møller and A. Kirrander, *J. Chem. Phys.*, 2019, **151**, 174302.

25 A. Föhlisch, P. Feulner, F. Hennies, A. Fink, D. Menzel, D. Sanchez-Portal, P. Echenique and W. Wurth, *nature*, 2005, **436**, 373–376.

26 R. Friend, D. Bradley and P. Townsend, *Journal of Physics D: Applied Physics*, 1987, **20**, 1367.

27 S. Bauch, L. K. Sørensen and L. B. Madsen, *Physical Review A*, 2014, **90**, 062508.

28 D. Popova-Gorelova and R. Santra, *Phys. Rev. B*, 2015, **92**, 184304.

29 T. Bredtmann, M. Ivanov and G. Dixit, *Nature Communications*, 2014, **5**, 5589.

30 J. Juse, D. Sundholm *et al.*, *Physical Chemistry Chemical Physics*, 1999, **1**, 3429–3435.

31 A. Amos and H. F. Roberts, *The Journal of Chemical Physics*, 1969, **50**, 2375–2381.

32 B. Stankus, J. M. Budarz, A. Kirrander, D. Rogers, J. Robinson, T. J. Lane, D. Ratner, J. Hastings, M. P. Miniti and P. M. Weber, *Faraday Discuss.*, 2016, **194**, 525–536.

33 B. Stankus, N. Zotev, D. M. Rogers, Y. Gao, A. Odate, A. Kirrander and P. M. Weber, *J. Chem. Phys.*, 2018, **148**, 194306.

34 T. J. A. Wolf, D. M. Sanchez, J. Yang, R. M. Parrish, J. P. F. Nunes, M. Centurion, R. Coffee, J. P. Cryan, M. Gühr, K. Hegazy, A. Kirrander, R. K. Li, J. Ruddock, X. Shen, T. Vecchione, S. P. Weathersby, P. M. Weber, K. Wilkin, H. Yong, Q. Zheng, X. J. Wang, M. P. Miniti and T. J. Martínez, *Nat. Chem.*, 2019, **11**, 504–509.

35 E. Itala, D. Ha, K. Kooser, M. Huels, E. Rachelew, E. Naummiste, U. Joost and E. Kukkk, *Journal of Electron Spectroscopy and Related Phenomena*, 2011, **184**, 119–124.

36 S. Sakai and S. Takane, *J. Phys. Chem. A*, 1999, **103**, 2878–2882.

37 W. C. Stolte and G. Öhrwall, *The Journal of chemical physics*, 2010, **133**, 014306.

38 B. Stankus, H. Yong, N. Zotev, J. M. Ruddock, D. Bellshaw, T. J. Lane, M. Liang, S. Boutet, S. Carbajo, J. S. Robinson, W. Du, N. Goff, Y. Chang, J. E. Koglin, M. P. Miniti, A. Kirrander and P. M. Weber, *Nature Chemistry*, 2019, **11**, 716–721.

39 H. B. Broughton and I. A. Watson, *Journal of Molecular Graphics and Modelling*, 2004, **23**, 51–58.

40 J. Jampilek, *MDPI*, 2019, **24**, 3839.

41 C. Lamberth, *Pest Management Science*, 2013, **69**, 1106–1114.

42 Y. Sanemitsu and S. Kawamura, *Journal of Pesticide Science*, 2008, **33**, 175–177.

43 S. K. Ahmed, W. B. Ali and A. A. Khadom, *International Journal of Industrial Chemistry*, 2019, **10**, 159–173.

44 A. Singh, K. R. Ansari, M. A. Quraishi, S. Kaya and P. Banerjee, *New J. Chem.*, 2019, **43**, 6303–6313.

45 S. V. Aradhya and L. Venkataraman, *Nature nanotechnology*, 2013, **8**, 399.

46 A. K. Ismael and C. J. Lambert, *Journal of Materials Chemistry C*, 2019, **7**, 6578–6581.

47 R.-H. Fan and X.-L. Hou, *The Journal of Organic Chemistry*, 2003, **68**, 726–730.

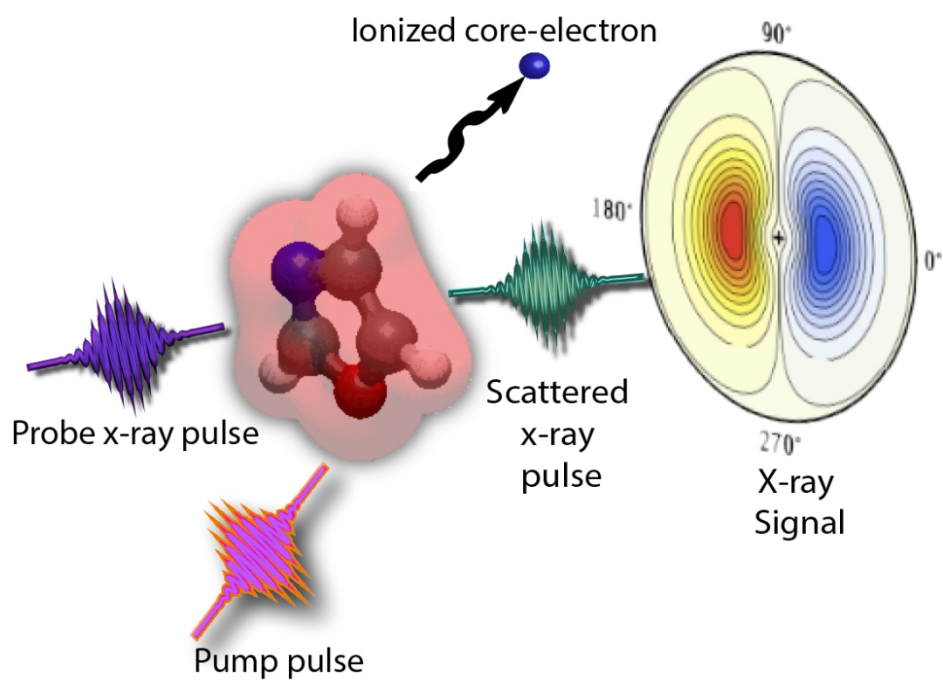
48 B. C. Arruda and R. J. Sension, *Phys. Chem. Chem. Phys.*, 2014, **16**, 4439–4455.

49 E. HAVINGA and J. Schlattmann, *Tetrahedron*, 1961, **16**, 146–152.

50 E. Izak-Nau, D. Campagna, C. Baumann and R. G. A. J. Polym. Chem., 2020, **11**, 2274–2299.

51 E. G. Robertson, *Journal of Molecular Spectroscopy*, 2005, **231**, 50–56.

- 52 T. Geng, J. Ehrmaier, O. Schalk, G. W. Richings, T. Hansson, G. Worth and R. D. Thomas, *The Journal of Physical Chemistry A*, 2020, **124**, 3984.
- 53 J. Cao, Z.-Z. Xie and X. Yu, *Chemical Physics*, 2016, **474**, 25–35.
- 54 H. Tanaka, T. Matsushita and K. Nishimoto, *Journal of the American Chemical Society*, 1983, **105**, 1753–1760.
- 55 T. Northey, N. Zotev and A. Kirrander, *J. Chem. Theory Comput.*, 2014, **10**, 4911.
- 56 A. M. Carrascosa and A. Kirrander, *Phys. Chem. Chem. Phys.*, 2017, **19**, 19545–19553.
- 57 G. Dixit, J. M. Slowik and R. Santra, *Phys. Rev. A*, 2014, **89**, 043409.
- 58 W. Schülke, *Electron Dynamics by Inelastic X-Ray Scattering*, Oxford Science Publications, 1st edn, 2007.
- 59 I. Waller and D. R. Hartree, *Proc. R. Soc. Lond. Ser.-A*, 1929, **124**, 119.
- 60 L. Bartell and R. Gavin, *J. Chem. Phys.*, 1965, **43**, 856–861.
- 61 R. A. Bonham and M. Fink, *High Energy Electron Scattering*, Van Nostrand Reinhold Company, ACS Monograph 169 edn, 1974.
- 62 A. Debnarova and S. Teichert, *J. Chem. Phys.*, 2006, **125**, 224101.
- 63 N. Zotev, A. Moreno Carrascosa, M. Simmermacher and A. Kirrander, *Journal of Chemical Theory and Computation*, 2020, **16**, 2594–2605.
- 64 R. M. Parrish and T. J. Martínez, *J. Chem. Theory Comp.*, 2019, **0**, null.
- 65 X. Li, N. Govind, C. Isborn, A. E. DePrince III and K. Lopata, *Chemical Reviews*, 2020, **120**, 9951–9993.
- 66 J. J. Goings, P. J. Lestrangle and X. Li, *Wiley Interdisciplinary Reviews: Computational Molecular Science*, 2018, **8**, e1341.
- 67 P. Krause, T. Klamroth and P. Saalfrank, *The Journal of chemical physics*, 2005, **123**, 074105.
- 68 J. A. Sonk, M. Caricato and H. B. Schlegel, *The Journal of Physical Chemistry A*, 2011, **115**, 4678–4690.
- 69 T. Sato and K. L. Ishikawa, *Physical Review A*, 2013, **88**, 023402.
- 70 D. R. Nascimento and A. E. DePrince III, *Journal of chemical theory and computation*, 2016, **12**, 5834–5840.
- 71 K. Lopata and N. Govind, *Journal of chemical theory and computation*, 2011, **7**, 1344–1355.
- 72 E. Runge and E. K. Gross, *Physical Review Letters*, 1984, **52**, 997.
- 73 J. Theilhaber, *Physical Review B*, 1992, **46**, 12990.
- 74 J. Sun, J. Song, Y. Zhao and W.-Z. Liang, *The Journal of chemical physics*, 2007, **127**, 234107.
- 75 A. Bruner, S. Hernandez, F. Mauger, P. M. Abanador, D. J. LaMaster, M. B. Gaarde, K. J. Schafer and K. Lopata, *The journal of physical chemistry letters*, 2017, **8**, 3991–3996.
- 76 M. R. Provorse, B. F. Habenicht and C. M. Isborn, *J. Chem. Theory Comput.*, 2015, **11**, 4791–4802.
- 77 J. I. Fuks, K. Luo, E. D. Sandoval and N. T. Maitra, *Phys. Rev. Lett.*, 2015, **114**, 183002.
- 78 E. Ruiz, S. Alvarez, J. Cano and V. Polo, *The Journal of chemical physics*, 2005, **123**, 164110.
- 79 J. P. Perdew and A. Zunger, *Physical Review B*, 1981, **23**, 5048.
- 80 L. S. Cederbaum and J. Zobeley, *Chemical Physics Letters*, 1999, **307**, 205–210.
- 81 A. I. Kuleff, N. V. Kryzhevoi, M. Pernpointner and L. S. Cederbaum, *Physical review letters*, 2016, **117**, 093002.
- 82 A. Sissay, P. Abanador, F. Mauger, M. Gaarde, K. J. Schafer and K. Lopata, *The Journal of chemical physics*, 2016, **145**, 094105.
- 83 P. Sándor, A. Sissay, F. Mauger, P. M. Abanador, T. T. Gorman, T. D. Scarborough, M. B. Gaarde, K. Lopata, K. J. Schafer and R. R. Jones, *Physical Review A*, 2018, **98**, 043425.
- 84 K. Lopata and N. Govind, *Journal of chemical theory and computation*, 2013, **9**, 4939–4946.
- 85 K. Lopata, B. E. Van Kuiken, M. Khalil and N. Govind, *Journal of chemical theory and computation*, 2012, **8**, 3284–3292.
- 86 A. Bruner, D. LaMaster and K. Lopata, *Journal of Chemical Theory and Computation*, 2016, **12**, 3741–3750.
- 87 M. Kadek, L. Konecny, B. Gao, M. Repisky and K. Ruud, *Physical Chemistry Chemical Physics*, 2015, **17**, 22566–22570.
- 88 T. S. Nguyen, J. H. Koh, S. Lefelhocz and J. Parkhill, *The Journal of Physical Chemistry Letters*, 2016, **7**, 1590–1595.
- 89 M. Chen and K. Lopata, *Journal of Chemical Theory and Computation*, 2020, **1**.
- 90 A. Szabo and N. S. Ostlund, *Modern Quantum Chemistry: Introduction to Advanced Electronic Structure Theory*, Dover Publishing Inc., 2nd edn, 1996.
- 91 J. Wang and V. H. Smith, *Int. J. Quant. Chem.*, 1994, **52**, 1145–1151.
- 92 W. C. Stolte, Y. Lu, J. A. Samson, O. Hemmers, D. L. Hansen, S. B. Whitfield, H. Wang, P. Glans and D. W. Lindle, *Journal of Physics B: Atomic, Molecular and Optical Physics*, 1997, **30**, 4489.
- 93 E. Apra, E. J. Bylaska, W. A. De Jong, N. Govind, K. Kowalski, T. P. Straatsma, M. Valiev, H. J. van Dam, Y. Alexeev, J. Anchell *et al.*, *J. Chem. Phys.*, 2020, **152**, 184102.
- 94 A. M. Carrascosa, H. Yong, D. L. Crittenden, P. M. Weber and A. Kirrander, *J. Chem. Theory Comp.*, 2019, **15**, 2836–2846.
- 95 D. A. Mazziotti, *Accounts of Chemical Research*, 2006, **39**, 207–215.
- 96 B. Stankus, H. Yong, J. Ruddock, L. Ma, A. M. Carrascosa, N. Goff, S. Boutet, X. Xu, N. Zotev, A. Kirrander, M. Miniti and P. M. Weber, *Journal of Physics B: Atomic, Molecular and Optical Physics*, 2020, **1**.
- 97 A. I. Kuleff, S. Lünemann and L. S. Cederbaum, *Chemical Physics*, 2013, **414**, 100–105.
- 98 F. Calegari, D. Ayuso, A. Trabatttoni, L. Belshaw, S. De Camillis, S. Anumula, F. Frassetto, L. Poletto, A. Palacios, P. Decleva *et al.*, *Science*, 2014, **346**, 336–339.
- 99 J. Breidbach and L. Cederbaum, *Physical review letters*, 2005, **94**, 033901.
- 100 E. Peretto, A. Trabatttoni, F. Calegari, M. Nisoli, A. Marini and G. Stefanucci, *The Journal of Physical Chemistry Letters*, 2020, **11**, 891–899.
- 101 L. Belshaw, F. Calegari, M. J. Duffy, A. Trabatttoni, L. Poletto, M. Nisoli and J. B. Greenwood, *The journal of physical chemistry letters*, 2012, **3**, 3751–3754.
- 102 A. M. Carrascosa, T. Northey and A. Kirrander, *Phys. Chem. Chem. Phys.*, 2017, **19**, 7853–7863.
- 103 T. Northey, A. M. Carrascosa, S. Schäfer and A. Kirrander, *J. Chem. Phys.*, 2016, **145**, 154304.



414x295mm (72 x 72 DPI)